



Inductive and Capacitive Hysteresis of Halide Perovskite Solar Cells and Memristors Under Illumination

Laura Munoz-Diaz^{1,2}, Alvaro J. Rosa¹, Agustín Bou¹, Rafael S. Sánchez¹, Beatriz Romero², Rohit Abraham John^{3,4}, Maksym V. Kovalenko^{3,4}, Antonio Guerrero^{1*} and Juan Bisquert^{1*}

¹Institute of Advanced Materials (INAM), Universitat Jaume I, Castellón de la Plana, Spain, ²Electronic Technology Area, Universidad Rey Juan Carlos, Móstoles, Spain, ³Department of Chemistry and Applied Biosciences, Institute of Inorganic Chemistry, ETH Zürich, Zürich, Switzerland, ⁴Empa-Swiss Federal Laboratories for Materials Science and Technology, Dübendorf, Switzerland

OPEN ACCESS

Edited by:

Moritz H. Futscher,
Swiss Federal Laboratories for
Materials Science and Technology,
Switzerland

Reviewed by:

Mengxia Liu,
Yale University, United States
Ho Won Jang,
Seoul National University, South Korea

*Correspondence:

Antonio Guerrero
aguerrer@uji.es
Juan Bisquert
bisquert@uji.es

Specialty section:

This article was submitted to
Solar Energy,
a section of the journal
Frontiers in Energy Research

Received: 06 April 2022

Accepted: 30 May 2022

Published: 19 July 2022

Citation:

Munoz-Diaz L, Rosa AJ, Bou A, Sánchez RS, Romero B, John RA, Kovalenko MV, Guerrero A and Bisquert J (2022) Inductive and Capacitive Hysteresis of Halide Perovskite Solar Cells and Memristors Under Illumination. *Front. Energy Res.* 10:914115. doi: 10.3389/fenrg.2022.914115

The current–voltage curves of memristors exhibit significant hysteresis effects of use for information storage and computing. Here, we provide a comparison of different devices based on MAPbI₃ perovskite with different contact configurations, from a 15% efficient solar cell to a pure memristor that lacks directional photocurrent. Current–voltage curves and impedance spectroscopy give insights into the different types of hysteresis, photacapitance, and inductance present in halide perovskites. It is shown that both halide perovskite memristors and solar cells show a large inverted hysteresis effect at the forward bias that is related to the presence of a chemical inductor component in the equivalent circuit. Based on the results, we classify the observed response according to recombination current in devices with selective contacts, to voltage-activated single-carrier device conduction in devices with symmetric contacts. These findings serve to gain an understanding of the mechanism of memristor currents in mixed ionic–electronic conductors such as halide perovskites. We establish the link in the electrical response between solar cells and memristors.

Keywords: perovskite, memristor, inverted hysteresis, impedance spectroscopy, solar cell

INTRODUCTION

Metal halide perovskite (MHP) is a promising photovoltaic technology that has produced very high efficiencies with solution-processed methodologies (Kim et al., 2020). MHPs can be described using an ABX₃ structure, where A = monovalent cations (i.e., methyl ammonium—MA), B = divalent cations (i.e., Pb²⁺), and X = halide anions (i.e., I[−]), with MAPbI₃ (MAPI) being the most studied configuration. In addition to remarkable electrooptical semiconductor properties, MHP semiconductors show mixed ionic–electronic conduction by ionic defect displacement (Azpiroz et al., 2015; Lopez-Varo et al., 2018; Senocrate and Maier, 2019; Zhang et al., 2020). This causes intrinsic memory effects (hysteresis) in the current–voltage (*I* – *V*) characteristics (Almora et al., 2016; Tress et al., 2016; Rong et al., 2017; Wu et al., 2018; Alvarez et al., 2020; Bisquert et al., 2021; Bisquert and Guerrero, 2022a) at both short and long time scales, forming an effective memristor. A memristor is a two-terminal device whose resistance depends on the history of current and voltage applied to the device. Memristors enable the storage of information by metastable modification of the device conductivity, (Pershin and Di Ventra, 2011; John et al., 2018a; Rahimi Azghadi et al., 2020; Fang et al., 2021; Kang et al., 2021; Kwak et al., 2021) and are the main candidates to realize artificial

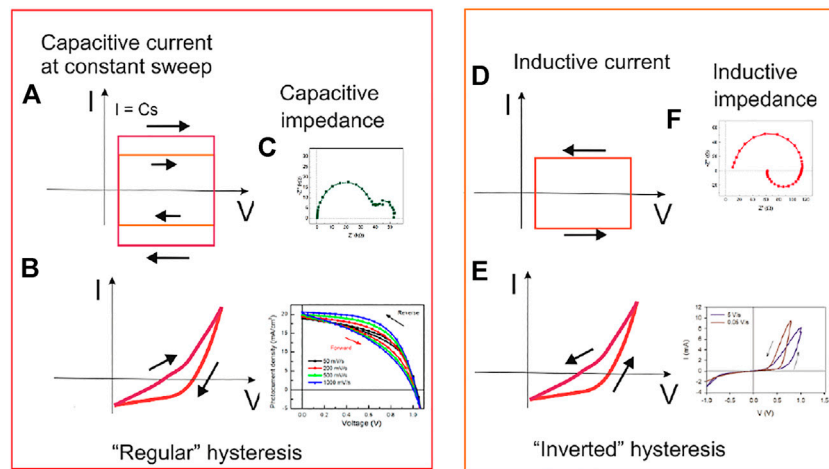


FIGURE 1 | Schematic response of impedance spectroscopy, current at constant sweep rate $V = st$, and hysteresis, for capacitive and inductive elements. The left panel shows the current of a constant capacitor (A), a diode with the capacitive response (B), and the impedance response (C). In the right panel, the signs and directions of the currents are schematically described for a system that is inductive at low frequency. In terms of the current-voltage (D), diode (E) and impedance (F) response.

synapses for neuromorphic computation algorithms (Mehonic and Kenyon, 2016; Rahimi Azghadi et al., 2020; John et al., 2021a; Bou and Bisquert, 2021; Gogoi et al., 2021; Gong et al., 2021; Kang et al., 2021; Kwak et al., 2021; Christensen et al., 2022). Arranged in a crossbar format with a differential configuration, memristors allow synaptic propagation to be realized facily via Kirchhoff's Current Law and Ohm's Law, enabling efficient in-memory computing (John et al., 2021b).

While conventional memristors are activated by purely electrical stimuli, photo-stimulation of memristive responses provides new opportunities for a variety of applications such as light-gated and electro-photo-sensitive memristors for optoneuromorphic and arithmetic computing, (Maier et al., 2016; Tan et al., 2017; John et al., 2018b; Emboras et al., 2020; John et al., 2020; Ma et al., 2021) integrated photonic neural networks, (Stark et al., 2020; Shastri et al., 2021), and preprocessing of image data in artificial vision before the transfer to the computing unit (Yang et al., 2020; Gong et al., 2021; Kim et al., 2021). Direct processing of visual information with such optoelectronic memristors may enable simpler architectures, mitigating the need for additional electro-optical converters for signal transduction and communication. MHPs are attractive materials for developing such novel electrooptical neuromorphic platforms because of their excellent optical absorption coefficient, charge transport, bandgap tunability extending across the UV, visible, and IR spectra, and high photoluminescence (PL) quantum yield, and high extinction coefficients. Combining these outstanding electronic properties with their intrinsic ionic conduction, MHPs would allow easy implementation of electrooptical synaptic elements for information storage and computing.

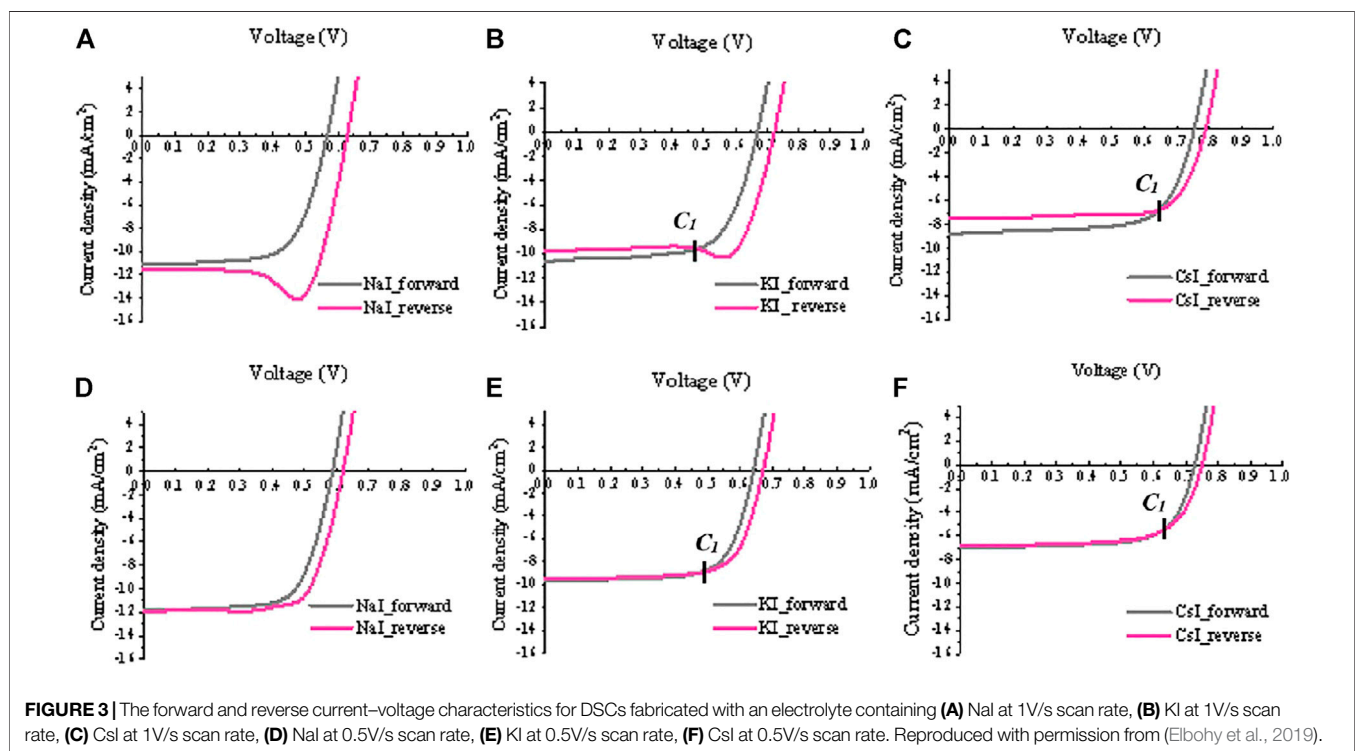
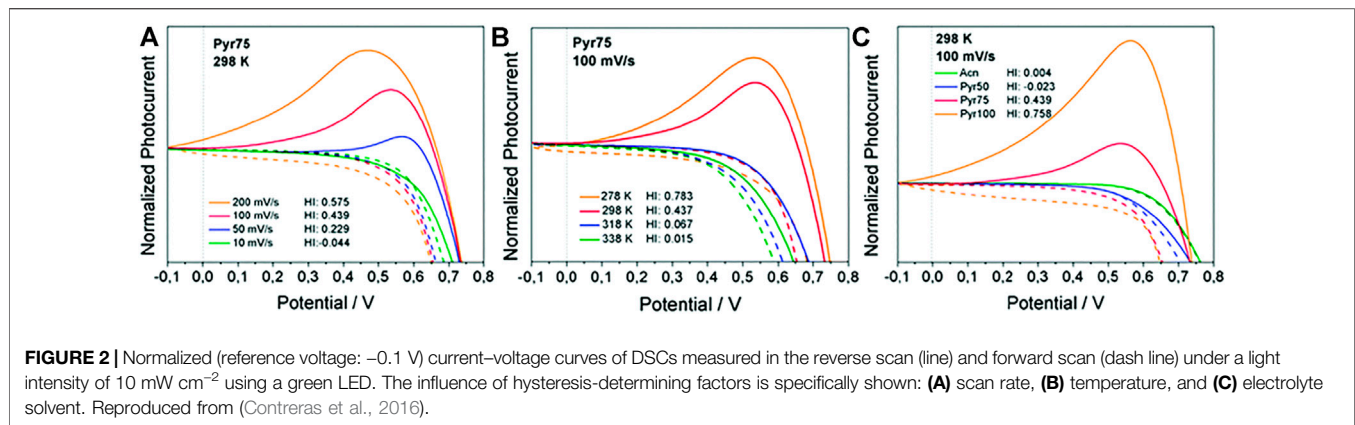
MHP memristors emerge from solar cells, but their behavior in the current-voltage regime is very different. In solar cells, the inverted hysteresis is a property preferably minimized (Tress et al., 2016; Yang et al., 2017; Wu et al., 2018), while for

memristors, it is amplified to permanent and reversible changes of the conductivity (Berruet et al., 2022). These characteristics have not been systematically studied yet, entailing significant attention.

Here, we aim to provide a clear understanding on the multiple features of the very complex $I - V$ curves of different devices and obtain fundamental insight about the ionic-electronic processes that cause the characteristics, in combination with insights from Impedance Spectroscopy (IS) measurements. We build different MHP formulation with low activation energy for ion migration that makes it suitable for memristor applications. First, we reproduce the standard solar cell (SC) configuration (FTO/c-TiO₂/m-TiO₂/MAPI/spiro-OMeTAD/Au). Two different MHP memristor devices are chosen for comparison as model systems that simplify the outer interfaces by removing the spiro-OMeTAD layer. The effect of the charge carrier selectivity of the perovskite/contact interface is studied by comparison with devices that contain PEDOT (FTO/PEDOT:PSS/MAPI/Au) and TiO₂ (FTO/c-TiO₂/mp-TiO₂/MAPI/Au). Measurements are completed in the dark and under illumination to show how the photovoltaic effects influence their operational properties. The present work establishes the link in the electrical response between solar cells and memristors. We unravel the poorly understood connection between the different regimes observed in the $I - V$ curve and the effect of light, first of its kind to the best of our knowledge.

HYSTERESIS OF CURRENT-VOLTAGE

Since the hysteresis of the current-voltage (Almora et al., 2016; Tress et al., 2016; Rong et al., 2017; Wu et al., 2018; Alvarez et al., 2020; Bisquert et al., 2021; Bisquert and Guerrero, 2022a) is a



central characteristic of the memristive devices, we summarize in **Figure 2** on the basic idea of capacitive and inductive hysteresis as described recently (Bisquert et al., 2021; Bisquert and Guerrero, 2022a). The type of hysteresis and IS response is highly connected with the presence of capacitive and inductive currents. The hysteresis is denoted “regular” as observed in solar cells when the current of the photovoltaic quadrant is more positive in the forward scan, **Figure 1B**. Alternatively, hysteresis is “inverted” as observed often in memristors when the positive current of the forward scan is lower than the positive current of the backward scan, **Figure 1D** (Li et al., 2022; Shen et al., 2017). Regular hysteresis has previously been correlated with the presence of capacitive behavior in the IS response while the inverted hysteresis indicates the presence of chemical inductors in the

response. The chemical inductor (Bisquert and Guerrero, 2022a) is a general denomination for a class of dynamical phenomena often based on a chemical reaction that produces a formal inductive response in impedance and transients without an underlying electromagnetic effect. The chemical inductor observed in halide perovskite solar cells is related to the slow ion-controlled electronic phenomena that occur at the interfaces of the devices. More details will be given in the following experiments.

We note that the hysteresis effects have been already observed in emerging solar cells, where ion motion is significant (Contreras et al., 2016; Elbohy et al., 2019). For example, the dye-sensitized solar cell contains a liquid electrolyte, and the strong capacitive hysteresis in $I - V$ curves is clearly observed in **Figure 2**, where

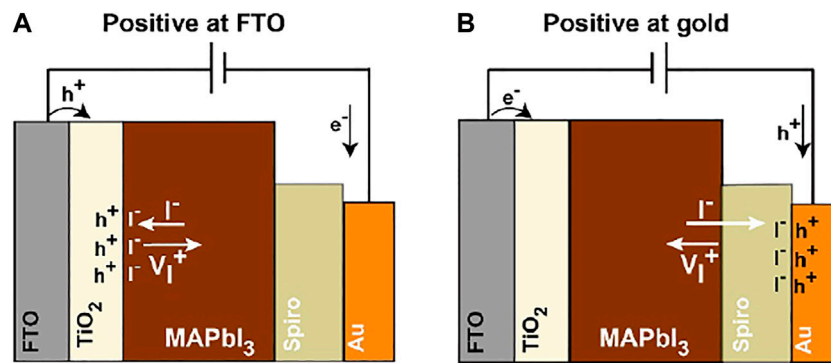


FIGURE 4 | Diagrams that show the TiO_2 and gold electrode polarization and direction of ion migration under a negative **(A)** and positive **(B)** bias in the dark, respectively, in MHP.

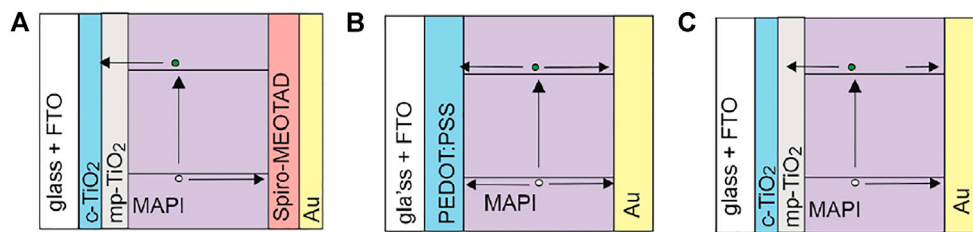


FIGURE 5 | Schematic of photogeneration of an electron-hole pair under illumination for **(A)** FTO/c- TiO_2 /m- TiO_2 /MAPI/spiro-OMeTAD/Au solar cell **(B)** optoelectronic FTO/PEDOT:PSS/MAPI/Au memristor device, **(C)** optoelectronic FTO/c- TiO_2 /mp- TiO_2 /MAPI/Au memristor device.

the effect of scan rate, temperature, and use of different solvents modify the hysteresis response. Similarly, the crossing effects in the $I - V$ curves of **Figure 3** show a transition between capacitive and inductive hysteresis that strongly depends on the mobile ionic species.

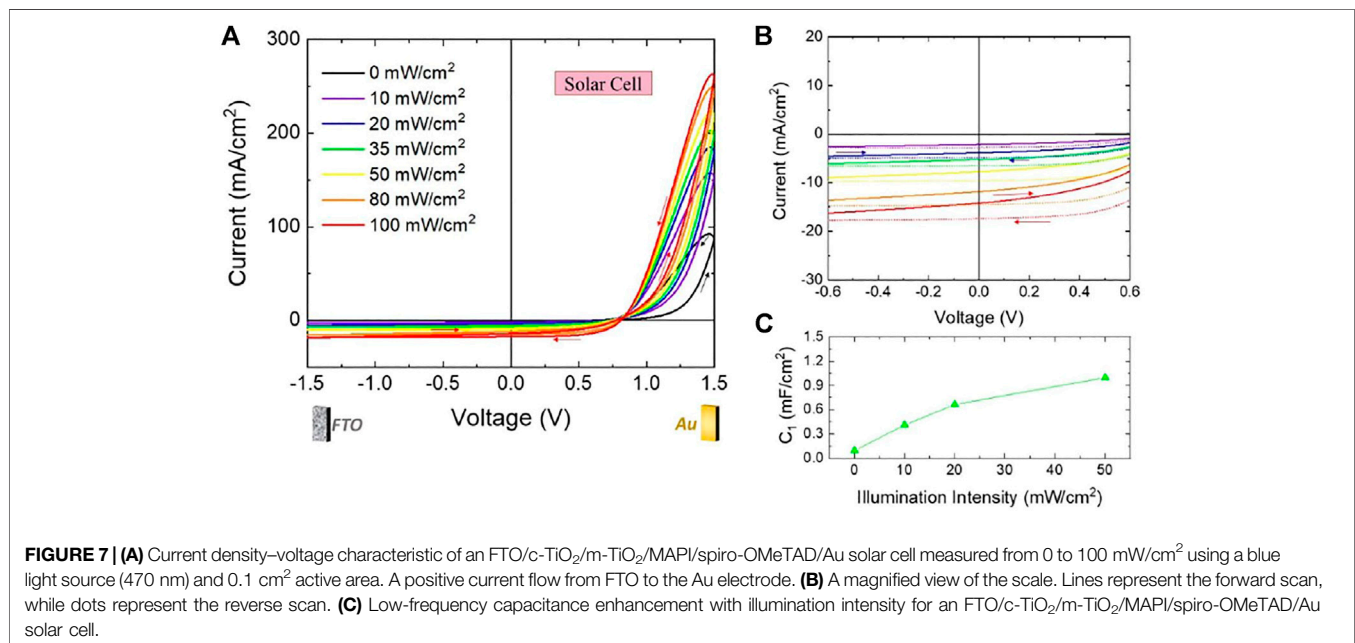
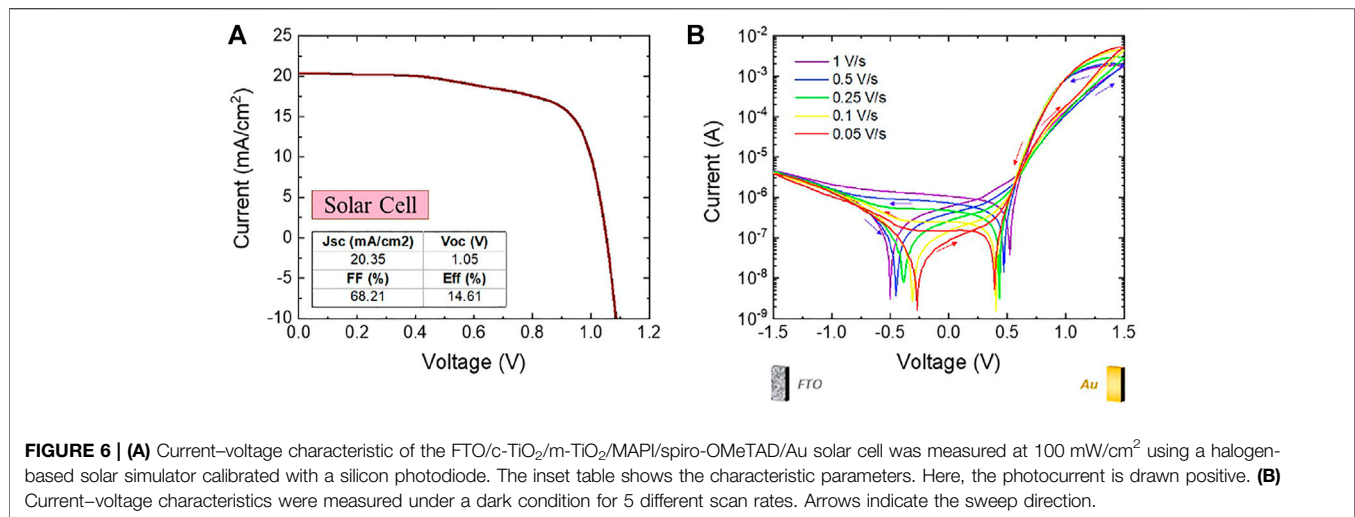
It has been reported that the resistive switching mechanism can be modified by using different top contacts (Han et al., 2019). Here, we focus on a low reactivity Au contact which is widely used in solar cells and the switching is controlled by the interface. In halide perovskite solar cells, migrating ions that reach the external contacts generate a capacitive current as the contacts compensate for their charge providing electroneutrality in the form of a capacitor (**Figure 4**). In MHP, this capacitance also depends on the light intensity with a rising light-induced capacitance, as previously reported (Juarez-Perez et al., 2014; Guerrero et al., 2021). It is known that halides vacancies (V_I^+), cations A (i.e., methyl ammonium), and metal collectors all can migrate at different rates under an external voltage bias. Halides vacancies are the fastest migrating species in MHP. When we apply a positive voltage at the FTO electrode (**Figure 4A**), halide vacancies will go toward gold and effectively create Γ^- excess concentration at the FTO/ TiO_2 interface. The opposite is true if we apply a positive voltage at the gold contact, **Figure 4B**. The capacitive and inductive effects of these ions at the interfaces can

be monitored by IS (Guerrero et al., 2021; Berruet et al., 2022; Taukeer Khan et al., 2022) as discussed in the latter sections.

RESULTS

The connection between light stimulation and production of photovoltage and photocurrent is well understood for a typical solar cell, **Figure 5A**. (Bisquert et al., 2004; Bisquert, 2020) Photogeneration in the semiconductor produces separated electron and hole carriers that diffuse to the metal collectors and the selectivity of contacts causes a directional photocurrent. When the voltage is increased in the forward direction, recombination is enhanced, and the photocurrent decreases until it vanishes at the open-circuit voltage (V_{oc}) point. In the reverse direction, there is a depletion of carriers which leaves only a small current, hence the solar cell shows a diode or rectification property. (Bisquert, 2020) However, a strong reverse bias may produce a breakdown effect with raising current in the opposite direction (Bowring et al., 2018).

Figure 6 shows the device configuration of the SC device and the electro-optical response. Our PV performance of $\sim 15\%$ is well aligned with reported values for the chosen formulation (**Figure 6A**). Hysteresis is typically observed in

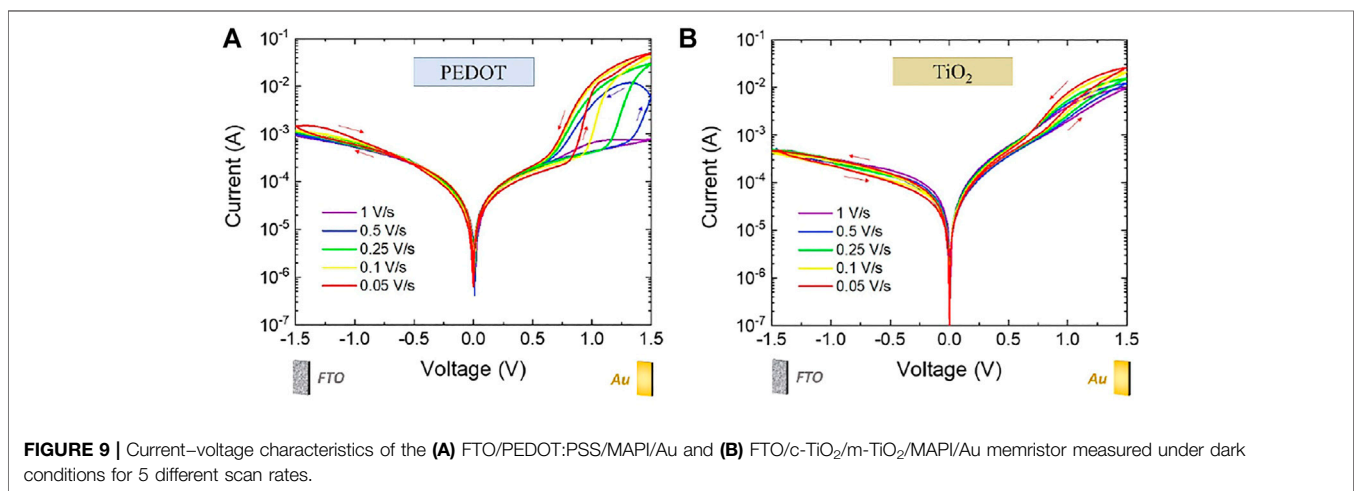
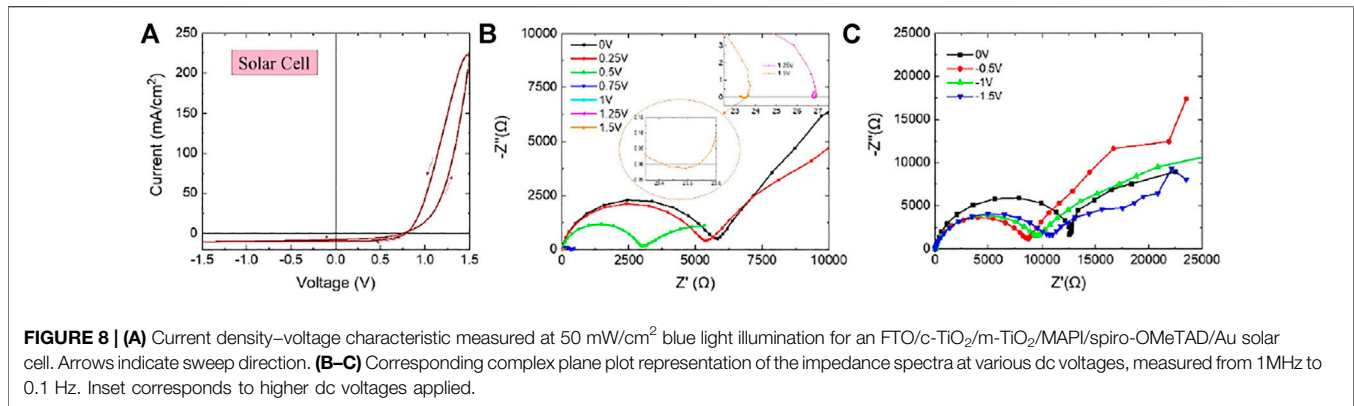


the current density–voltage ($j-V$) curve for this configuration with separation of the forward and backward scans even for measurements conducted in dark (**Figure 6B**). The hysteresis behavior is complex with marked differences as a function of the scan rates, presence of crossing points of the curves at about +0.6 V, and change in the sign of the current far away from 0 V (spikes in the semilog curves) (Li et al., 2022).

Figure 7 shows photovoltaic performance of the solar cell device under a monochromatic blue light at different illumination intensities, with negative current for photovoltaic effect. As expected, the photogenerated current is enhanced with light intensity thanks to the excellent carrier generation and extraction. Very interestingly, in the complete SC there is a crossing in the forward and reverse scans at V_{oc} conditions

with a change in tendency from regular ($V < V_{oc}$) to inverted ($V > V_{oc}$) hysteresis. In addition, the capacitive hysteresis also increases with illumination level in terms of the separation of the forward and reverse scan on the y-axis (**Figure 7B**). The capacitance takes values in the order of 0.2–0.9 mF/cm².

Figure 8 shows the $j-V$ characteristic of the solar cell device at 50 mW/cm² blue light illumination. Below V_{oc} , the capacitive behavior shows regular hysteresis and above V_{oc} the inductive behavior is manifested in the $j-V$ as inverted hysteresis as in **Figure 7A**. **Figures 8B,C** confirm this statement, showing two capacitive arcs in the complex plane plot. Only at high dc voltages, beyond V_{oc} , it is possible to observe an inductive behavior (Bisquert and Guerrero, 2022a; Berruet et al., 2022), with low frequencies crossing to the fourth quadrant of the complex plane (**Figure 8B** inset). We note that the inductive



loop is not well developed as in the next experiments clearly indicating that spiro-OMeTAD is affecting the impedance response.

The model systems which do not contain spiro-OMeTAD have been fully characterized with two types of selective contacts, PEDOT:PSS (selective to holes), and TiO₂ (selective to electrons). The dark $I-V$ characteristics of the two memristor devices at different voltage sweep rates are shown in **Figure 9**. Memristor performance of the device containing Spiro-OMETAD is well aligned with previously reported results (Berruet et al., 2022). Both show inverted hysteresis loops when the voltage is positive at the Au contact similar to the SC configuration above ~ 0.5 V in **Figure 7A**. The onset voltage for transition to the higher conductance state is larger for higher sweep rates, as explained in a recent work (Berruet et al., 2022) that will be summarized in the Model section. The loop is steeper for the PEDOT memristor, due to the fact that the compact/mesoporous TiO₂ is a better selective contact for electrons than PEDOT, which reduces the hysteresis effect in the TiO₂ memristor case. We note that some of the most recent reported memristors show performances higher than those reported here. However, top performance devices contain buffer layers (i.e., PMMA) at both perovskite/contact

interfaces and reactive contacts (i.e., Ag) that complicate the device configuration and interpretation of operational mechanism. Here, we work with a simplified configuration to provide an understanding of the operational mechanism of memristors and devices that have been fabricated without a buffer layer in the perovskite/top contact interface.

It is also important to highlight that the response in the dark is only inductive at positive voltages, there is no crossing for both model systems as compared to the SC for measurements in the dark. This result clearly points to the capacitive currents due to the migrating Γ^- ions with Spiro-OMETAD in the dark of the SC configuration. Otherwise, only PEDOT memristors show inverted hysteresis when the voltage is negative. For TiO₂ memristors, the capacitive hysteresis is found in this region, as shown in solar cell devices in **Figure 7B**. This difference in PEDOT memristor performance is due to irreversible reactions taking place between ions and TiO₂ at this interface. For example, for the interface TiO₂/MAPI it has been reported that Ti–I–Pb bonds may form, as identified by Raman Spectroscopy, which can easily accommodate excess ionic charge when a negative bias is applied (Carrillo et al., 2016). This configuration could lead to neutral interfaces that would be in agreement with the low

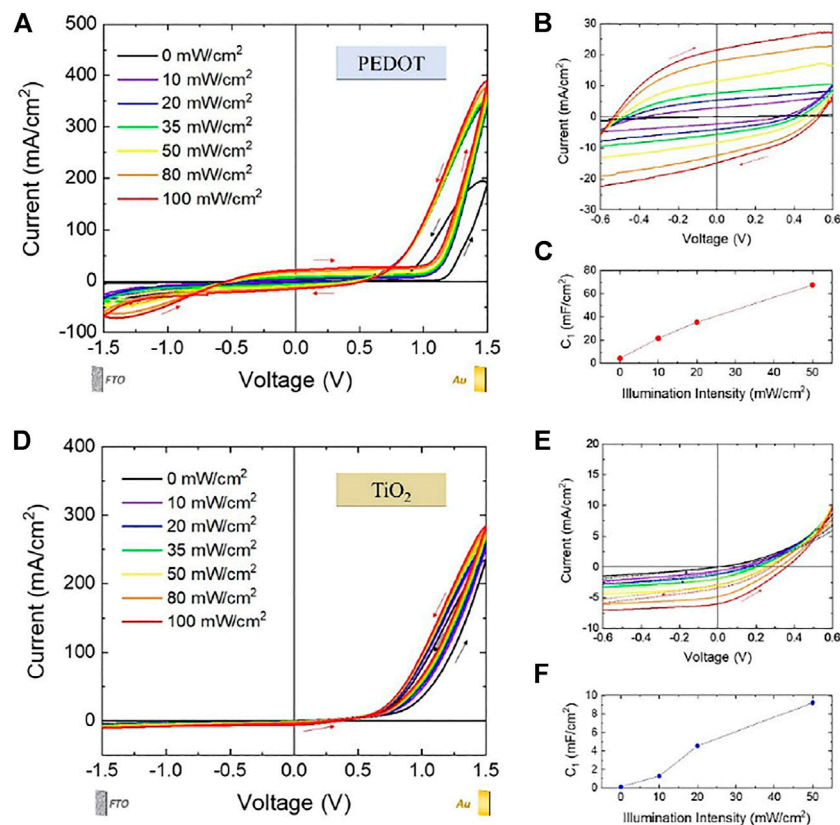


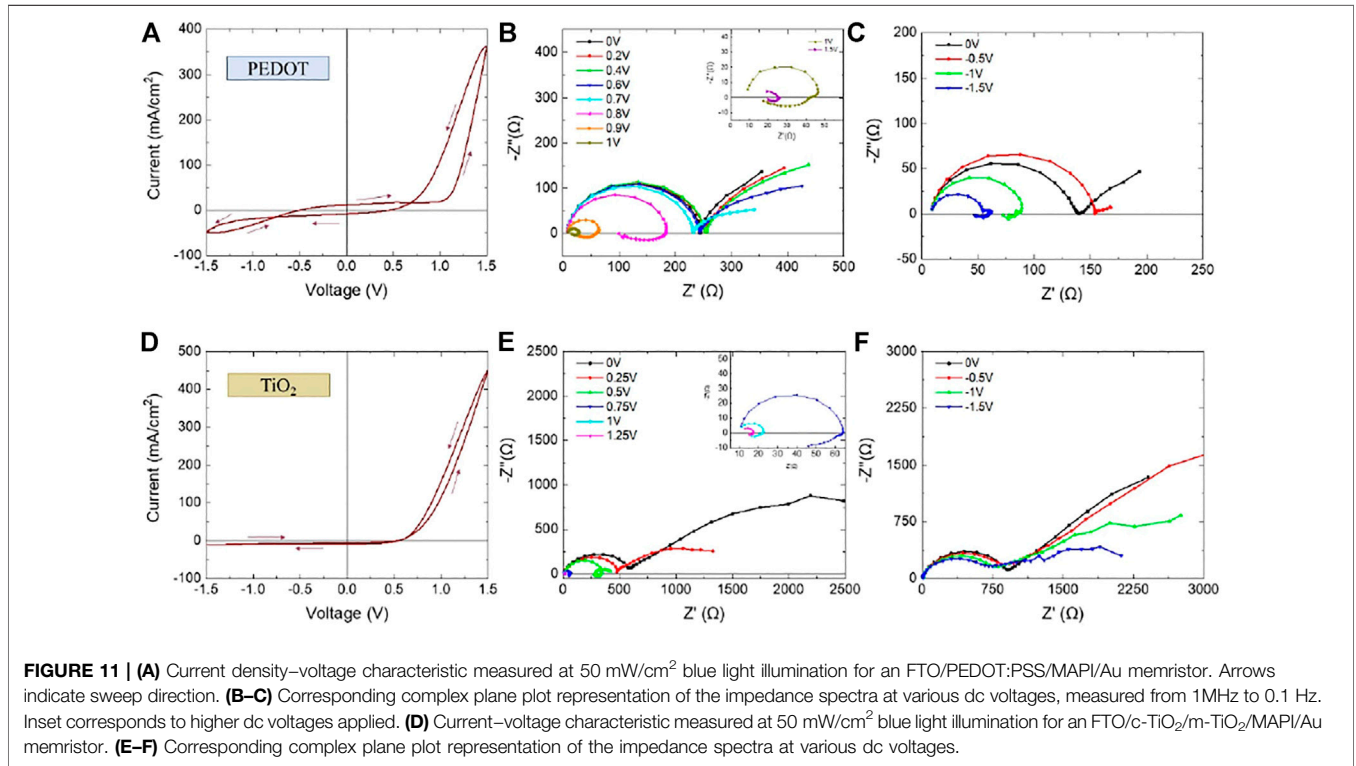
FIGURE 10 | (A) Current density–voltage characteristic of an FTO/PEDOT:PSS/MAPI/Au memristor measured from 0 to 100 mW/cm² using a blue light source (470 nm) and 0.1 cm² active area. **(B)** A magnified view of the scale. **(C)** Low-frequency capacitance enhancement with illumination intensity for an FTO/PEDOT:PSS/MAPI/Au memristor. **(D)** The current density–voltage characteristic of an FTO/c-TiO₂/m-TiO₂/MAPI/Au memristor was measured at different illumination intensities. Panel **(E)** corresponds to a magnified view of the scale. Lines represent the forward scan and dots represent the reverse scan. **(F)** Corresponding low-frequency capacitance variation with illumination intensity.

capacitance measured in the current work for the memristor containing TiO₂. Comparing these characterizations with the one previously discussed in **Figure 6B**, it is possible to affirm that the TiO₂ device shows closer performance to an MHP solar cell than the PEDOT device in dark conditions.

To investigate the effect of light on the memristor devices, we performed the current-voltage characterization at different illumination levels and the results are shown in **Figure 10**. In principle, the looping curves are like those in the dark in **Figure 9**. But there are also significant differences. The PEDOT device shows a symmetric opening of the curves $V = 0$ for increasing light intensity, **Figure 10B**. This is the effect of the light-induced capacitance, previously mentioned, that is well known in halide perovskites (Juarez-Perez et al., 2014). Indeed, the measured capacitance increases with light intensity as indicated in **Figure 10C**. For the TiO₂ device, the photoinduced capacitive current is also observed, but it is clearly displaced to negative values of the current since the TiO₂ is selective to electrons and it is able to extract the photogenerated current. In consequence, the TiO₂ device shows diode-like characteristics and a positive

photovoltage at all light intensity values. The difference between the two devices is explained by the mechanistic diagrams in **Figure 5**. The PEDOT device has a negligible effect on contact selectivity, hence capacitive current prevails in the photocurrent. For TiO₂ devices, the metal oxide contact acts as a selective contact that extracts preferentially electrons, hence the photogeneration gives a dominant-negative photocurrent for both signs of the voltage sweep direction. Thus, this performance is similar to the one developed by a solar cell, shown in **Figure 7A**.

For further analysis, we focus on a particular illumination, **Figure 11**. For PEDOT devices, it is observed that there are two loops on right and left of **Figure 11A**, where the current in forward and backward makes crossing pathways. As mentioned earlier in **Figure 3** this property indicates a change from regular to inverted hysteresis caused by the onset of dominant inductive property in the impedance spectra (Bisquert and Guerrero, 2022a; Berruet et al., 2022). The presence of the chemical inductor (the loop in the fourth quadrant of the complex plane) is in fact obtained in the



measurements of impedance spectroscopy in **Figures 11B,C**. While this change from capacitive to inductive behavior is shown in **Figure 11E** at high positive voltages, this is not obtained when negative voltages are studied in TiO₂ memristors (**Figure 9B**), corresponding with the loops in **Figure 8D**. This trend is similar to the one shown by the solar cell device, **Figures 8B,C**, with inductive properties significant only at high dc voltages.

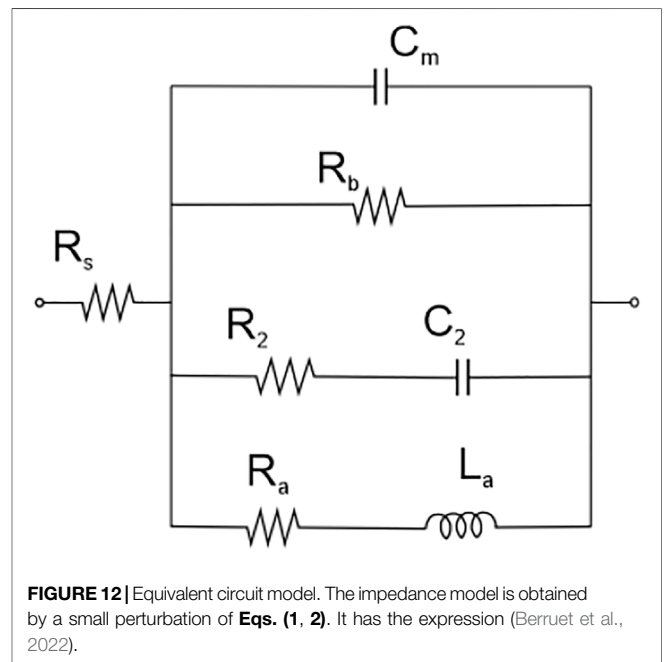
MODEL

In order to explain the experimental observations in a unified framework, we present a dynamical model (Berruet et al., 2022) that includes several capacitive mechanisms and a chemical inductor feature. It is formed by the system of equations

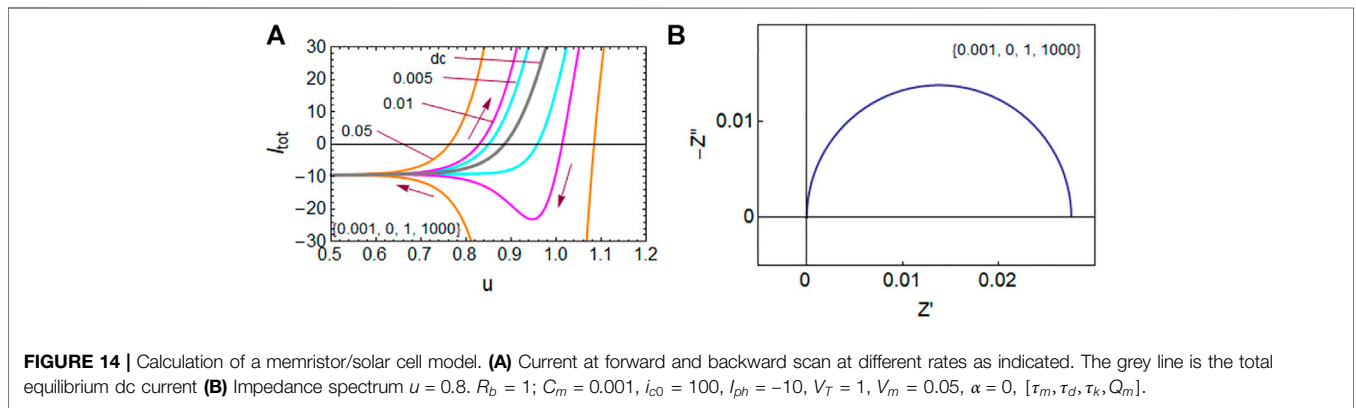
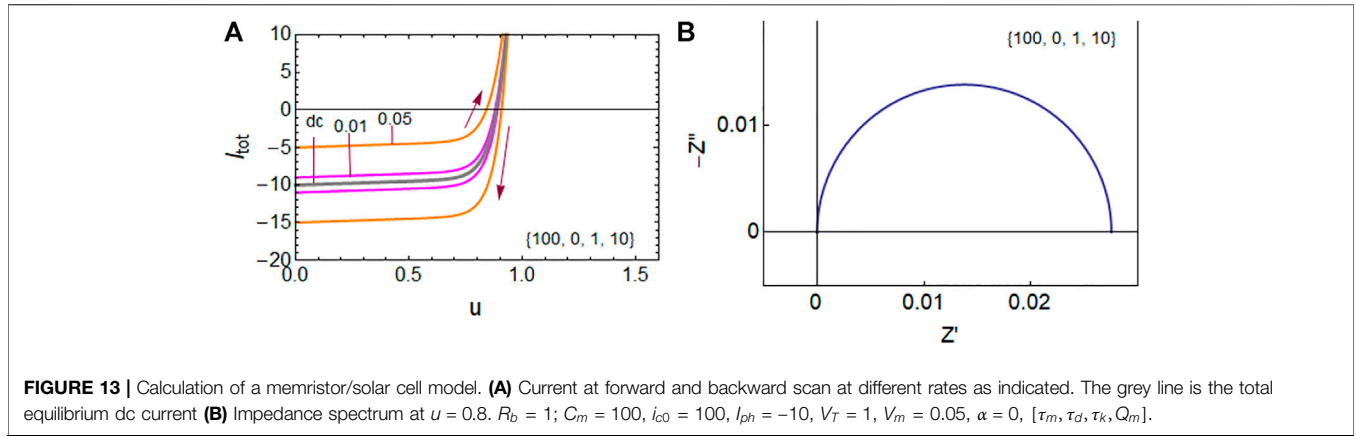
$$I_{tot} = I_{ph} + i_{c0}f + \frac{u}{R_b} + C_m \frac{du}{dt} + Q_m \frac{df}{dt}, \quad (1)$$

$$\tau_k \frac{df}{dt} = (1 - f) - e^{-\frac{u-V_T}{V_m}} f. \quad (2)$$

The model has three independent variables: I_{tot} , u , f . The first two are the external current and voltage and f is an occupation function ($0 \leq f \leq 1$). The variable f indicates the state of the mechanism that controls the large injection current in the activated state, with the onset potential V_T . V_m is an ideality factor with a dimension of voltage. i_{c0} is the saturation value of the injection current. Our model provides an alternative pathway to those approaches based on drift-diffusion simulations.



(Li et al. 2022; Shen et al., 2017) This simple two-dimensional model already describes simultaneously the current-voltage curves and impedance characteristics. Furthermore, the model enables full analysis of time transient techniques. (Bisquert and Guerrero, 2022b).



Eq. 1 describes the components of I_{tot} : the photocurrent I_{ph} , the injection current $i_{c0}f$, a small ohmic current of constant resistance R_b , a capacitive charging of the interfaces with capacitance C_m , and a voltage-dependent capacitance correlated to f with a maximum surface charging Q_m .

If the time derivative in **Eq. 2** is suppressed, we obtain the following steady-state solution:

$$f_{ss}(u) = \frac{1}{1 + e^{-(u-V_T)/V_m}}. \tag{3}$$

Eq. 2 is a delay equation that states that the formation of the conduction state at a certain voltage, $f_{ss}(u)$, lags behind the changes of applied voltage with a characteristic time τ_k . This slowing down of the response gives rise to the chemical inductor in the equivalent circuit.

The steady-state current is

$$I_{app} = I_{ph} + \frac{u_{app}}{R_b} + i_{c0}f_{ss}(u). \tag{4}$$

In the solar cell a saturation regime $f_{ss} \approx 1$ may not be observed. Then the current in the injection regime at large voltage has the exponential form

$$I_{app} \approx I_{ph} + i_{rec0}e^{u_{app}/V_m}, \tag{5}$$

where i_{rec0} is a recombination current parameter. The impedance model is obtained by small perturbation of **Eqs. (1, 2)**. It has the expression (Berruet et al., 2022).

$$Z(s) = \left[C_m s + R_b^{-1} + \frac{1}{R_a + L_a^k s} + \frac{1}{R_2 + \frac{1}{C_2 s}} \right]^{-1}, \tag{6}$$

$$R_a^{-1} = \frac{di_c}{du} = \frac{i_{c0}}{V_m} f_{ss} (1 - f_{ss}), \tag{7}$$

$$L_a^d = \tau_d R_a, \tag{8}$$

$$R_2 = \frac{L_a^k i_{c0}}{Q_m}, \tag{9}$$

$$C_2 = \frac{Q_m}{R_a i_{c0}}. \tag{10}$$

The equivalent circuit is shown in **Figure 12**.

Based on this model we can form several regimes of responses observed in the experimental evidence of the preceding Section.

In **Figure 13** we show the effect of a constant capacitor C_m that opens the steady-state $I - V$ in capacitive hysteresis as in **Figures 1, 7B**. **Figure 14** shows the effect of voltage-activated capacitor C_2 that becomes active at V_{oc} . It causes capacitive spikes close to V_{oc} as in **Figures 2, 3A**.

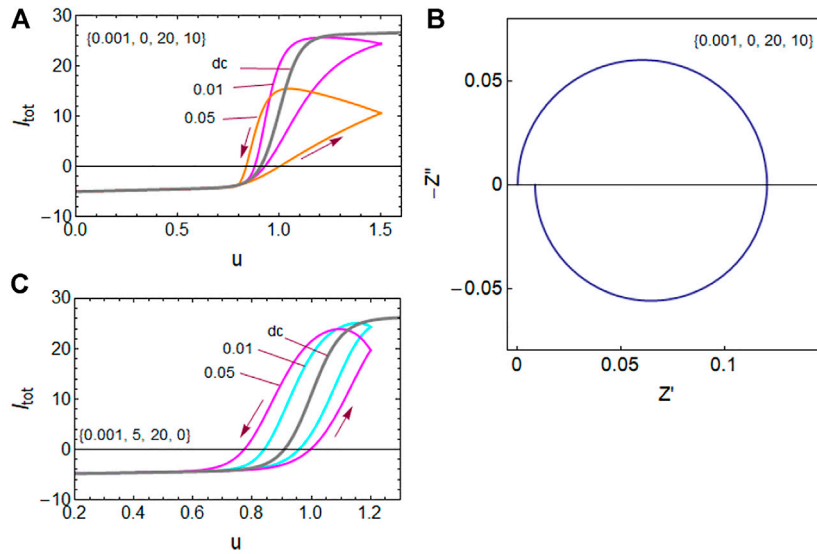


FIGURE 15 | Calculation of a memristor/solar cell model. **(A)** Current at forward and backward scan at different rates as indicated. The grey line is the total equilibrium dc current **(B)** Impedance spectrum at $u = 0.95$. $R_b = 1$; $C_m = 0.001$, $i_{c0} = 100$, $I_{ph} = -10$, $V_T = 1$, $V_m = 0.05$, $\alpha = 0$, $[\tau_m, \tau_d, \tau_k, Q_m]$. **(C)** Current at forward and backward scan at different rates as indicated. $R_b = 1$; $C_m = 0.001$, $i_{c0} = 30$, $I_{ph} = -10$, $V_T = 1$, $V_m = 0.05$, $\alpha = 0.5$, $[\tau_m, \tau_d, \tau_k, Q_m]$.

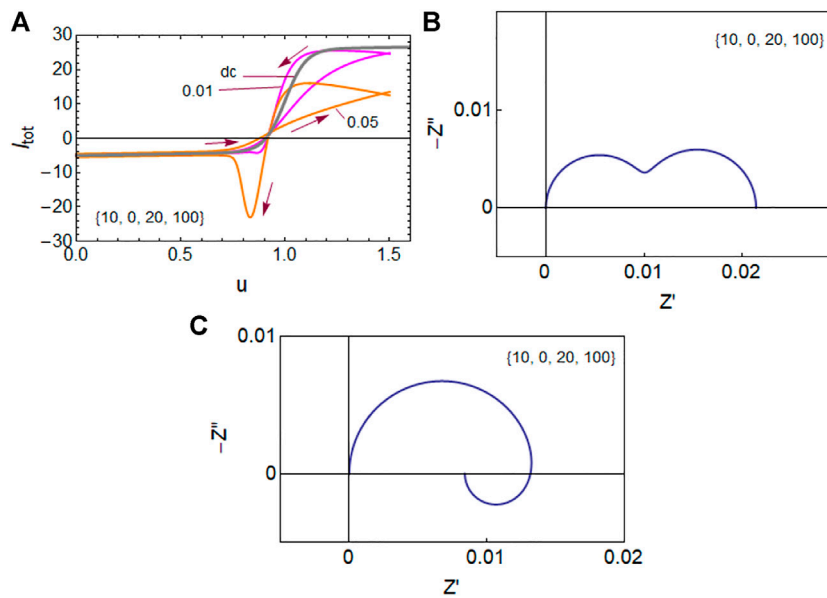


FIGURE 16 | Calculation of a memristor/solar cell model. **(A)** Current at forward and backward scan at different rates as indicated. The grey line is the total equilibrium dc current **(B)** Impedance spectrum at $u = 0.88$ and **(C)** $u = 0.95$. $R_b = 1$; $C_m = 10$, $i_{c0} = 100$, $I_{ph} = -5$, $V_T = 1$, $V_m = 0.05$, $\alpha = 0$, $[\tau_m, \tau_d, \tau_k, Q_m]$.

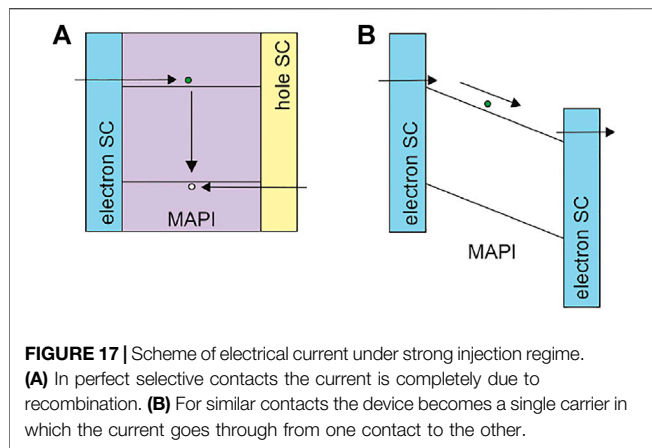
Figure 15A shows the inductive hysteresis loop that is observed at a large injection current in the measuring devices. To provide a more complete description of the inductive hysteresis we extend the model as follows:

$$I_{tot} = I_{ph} + \frac{u}{R_b} + i_c + C_m \frac{du}{dt} + Q_m \frac{df}{dt}, \quad (11)$$

$$\tau_d \frac{di_c}{dt} = i_{c0} f - i_c, \quad (12)$$

$$\tau_k \frac{df}{dt} = e^{\frac{u-V_T}{V_m}} (1-f) - e^{(\alpha-1)\frac{u-V_T}{V_m}} f. \quad (13)$$

This more general three-dimensional model has four independent variables: I_{tot} , u , f , i_c . Here the injection current



i_c is a variable in addition f . In steady-state, they satisfy the relationship

$$i_c = i_{c0} f_{ss}. \quad (14)$$

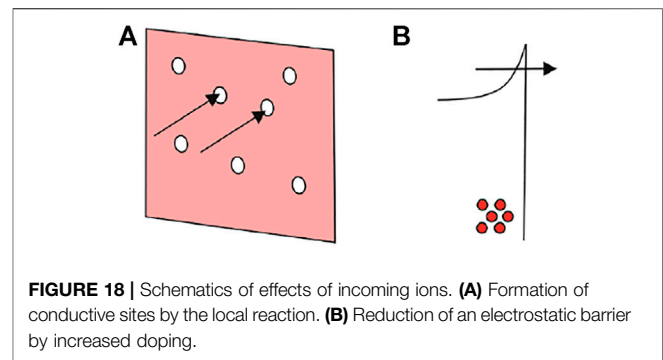
As described before (Berruet et al., 2022), Eq. 12 represents a diffusion or migration time of ions that introduces a delay i_c with respect to the external perturbation, by the characteristic time constant τ_d . This temporal parameter indicates the time necessary to establish the configuration of high f that produces the large electronic current i_{c0} . Eq. 13 is an extension of (2) with a Tafel coefficient α . It is observed in Figure 15C that the expanded model provides different shapes in which the go and return currents make parallel tracks.

Finally, in Figure 16 the capacitive hysteresis is combined with an inductive hysteresis at high voltage. There is a crossing point from capacitive to inductive hysteresis in Figure 16, as observed in Figure 7A. In the impedance spectra, the low-frequency capacitive arc is transformed into an inductive feature in the fourth quadrant of the complex plane.

DISCUSSION

The previous analysis shows that a voltage-activated current with capacitive and inductive kinetic properties provides a satisfactory explanation of the current-voltage hysteresis and impedance properties of the different devices studied. We obtained a good description of the experimental results. Models with very few variables describe a large span of observed phenomena. The question is to give a definitive interpretation to the transformation equations in terms of physical mechanisms. One recent example is the combination of bidirectional photocurrent and hysteresis that has been discussed by modification of the contact layer. (Li et al. 2022).

We considered three types of devices: a solar cell with excellent selective contacts, a PEDOT memristor with both contacts selective to holes, and a hybrid TiO₂ device with partially selective contacts. In Figure 5 we showed elementary models to explain the mechanism under light



conditions close to zero applied voltage that leads to the generation of a photocurrent. In the experimental figures, we have observed the transition to a large current when the Au electrode is positively biased. This large current and the associated memory effect is the key operational characteristic of a memristor. In addition, we showed that the presence of regular/capacitive hysteresis under illumination is connected with the surface ionic polarization by the high capacitance measured by IS and the large capacitive current that scales with the light intensity.

Alternatively, for measurements in the dark, large inductive currents have been observed in all types of devices measured. We can discuss the origin of the large current rise in the dark injection regime based on Figure 17.

In the case of a solar cell with very good selective contacts, the large current is due to recombination as shown in Figure 17A. This current regime is usually not analyzed in solar cells as the regime beyond V_{oc} is uninteresting compared to the extraction regime below V_{oc} . However, we have shown in the previous sections that the exponential current is well described by Eq. 5 as a recombination current that may correspond to electron-hole recombination via trap states as often reported for Light Emitting Diodes. Numerous analyses have discussed the effective ideality factor in relation to the recombination mechanisms. (Wetzelaer et al., 2015; Tress et al., 2018; Caprioglio et al., 2019).

For the operation of memristors, the injection domain is an important feature of the device operation. It is therefore essential to obtain a physical description of the variable f that provides the exponential rise of the injection current at a certain voltage. Based on the model discussion, we have several options:

- 1) The memristor device injects electrons and holes by partially selective contacts as in Figure 17A, producing a recombination current and f representing the ion-activated recombination sites as suggested in solar cells (Pockett and Carnie, 2017; Shen et al., 2017).

But another possibility is that there is no contact selectivity and the current is due to just one carrier going through the sample as in Figure 17B, i.e., electron-only devices. (Li et al., 2022) In the current work both PEDOT:PSS and Au are contacted more selective to holes than electrons due to

their energy levels and have often been used for this purpose in solar cells and LEDs research. Therefore, it is likely that if the second possibility is responsible for the inductive currents and the device would be hole-only. The question is to determine the physical origin of the activation function f in this case. The activation mechanisms must predict an exponential rise and a saturation effect. There are several options outlined in **Figure 18**:

- 2) The activation of surface conduction sites by reaction of the incoming ions, **Figure 18A**. Here is the interpretation of the function f in **Eqs. 1–2** is direct: It is the fraction of surface-activated sites. The chemistry of the perovskite/contact perovskite is very complex and it is possible that the presence of halides at the interface and oxidizing/reducing conditions may lead to the formation/rupture of electrically conductive sites. A representative example is the case of the interface MAPI/Au where gold halides (i.e., AuI₃) may form reversibly during polarization at positive bias and create an interface with reduced resistance to extract the charge (Pospisil et al., 2019). A negative bias, metallic Au would be recovered with increased charge transfer resistances. A similar, effect has been reported for devices containing MAPI/Ag (Solanki et al., 2020).
- 3) The decrease of an electronic surface barrier between the perovskite layer and the contacts, **Figure 18B** (Yang et al., 2013). This is caused by changes in doping ions around the interface, in a Schottky barrier diode mechanism.
- 4) A filamentary conductive pathway through the perovskite layer, is the standard mechanism of high current in memristors (Fang et al., 2021).

The present experimental results and modeling do not distinguish between these options, or between models in **Figure 17** and **Figure 18**, and additional discriminatory experimental work is needed.

CONCLUSION

The operation of solar cells and memristors depends crucially on the structure of contacts. We found different phenomena like directional photocurrent, photocapacitance at low bias voltage, and alternation of capacitive and inductive hysteresis domains can be explained by a model in which the rising current is activated by voltage. In the case of a solar cell, this current is well explained by the ionic-dependent recombination model. But for the memristor, different options appear since the devices are less affected by photogeneration and may become single carrier dominated. We conclude that solar cells and memristors can have very different underlying mechanisms, but more investigation is

needed for the attribution of the rising current and the memory effect.

EXPERIMENTAL

Device Fabrication

All materials and solvents were used as received. FTO glass (Pilkington TEC 15), PEDOT:PSS (Heraeus CLEVIOS™ P VP AI 4083), titanium diisopropoxide bis(acetylacetonate) (Merk, 75% solution in 2-propanol), absolute ethanol (Sigma Aldrich, anhydrous 99.8%), acetylacetone (Sigma Aldrich, 99%), TiO₂ paste (Dyesol, DSL 18NR-T), CH₃NH₃I (MAI, Greatcellsolar), PbI₂ (TCI, 99.99%), DMF (Sigma Aldrich, anhydrous 99.8%), DMSO (Sigma Aldrich, anhydrous 99.9%), chlorobenzene (Sigma Aldrich, 99.8%), spiro-OMeTAD (Sigma Aldrich, anhydrous 99%), LITBSF (Sigma Aldrich, anhydrous 99.95%), Acetonitrile (Sigma Aldrich, anhydrous 99.9%), 4-tert-butylpyridine (TBP) (Sigma Aldrich, 99.8%). The precursor solution for the compact layer of TiO₂ (c-TiO₂) was prepared by mixing 0.4 ml of acetylacetone and 0.6 ml of titanium diisopropoxide bis(acetylacetonate) in 9 ml of absolute ethanol. In order to prepare mesoporous TiO₂ layer precursor, 150 mg of TiO₂ paste is required for each milliliter of ethanol. The MAPbI₃ precursor solution is prepared by preparation of DMF solutions (50 wt%) containing MAI and PbI₂ (1:1 mol%) and MAI, PbI₂, and DMSO (1:1:1 mol%) as reported previously. Briefly, MAI (235 mg) and PbI₂ (681.5 mg) were mixed in DMF (1 ml) and DMSO (95 μL). Spiro-OMeTAD solution requires 72.3 mg of spiro-OMeTAD for each milliliter of chlorobenzene. Then, 17.5 μL of LITBSF solution (520 mg of Li⁺ salt per milliliter of acetonitrile) and 28.8 μL of TBP must be added.

Devices were prepared following previously reported methods. (Aranda et al., 2017) All devices were prepared starting from FTO glass substrates. Etching was carried out with zinc powder and HCl solution (2 M). Afterward, samples were brushed, cleaned with Hellmanex solution, and rinsed with Milli-Q water. For a complete cleaning, the substrates were sonicated in acetone for 15 min and this step was repeated with a mixed 50:50 ethanol-isopropanol solution. Finally, substrates were dried with nitrogen and treated in a UV–O₃ chamber for 15 min. For PEDOT-based memristors, PEDOT:PSS solution was filtered using PTFE 0.45 μm syringe filter and spin-coated on the substrate at 3000 rpm for 30 s. This was followed by annealing at 120°C for 10 min. Alternatively, for TiO₂-based devices, a compact TiO₂ layer was deposited at 450°C by aerosol spray pyrolysis. The solution was sprayed using pure oxygen as a carrying gas and annealing was carried out at 450°C for 30 min. The mesoporous TiO₂ layer was spin-coated at 2000 rpm for 10 s and annealed following several temperature steps. Devices were transferred to a nitrogen-filled glovebox, samples are

heated at 100°C for 5 min to avoid residual humidity on their surface. The perovskite precursor solution was spin-coated at 4000 rpm for 50 s, using chlorobenzene as an antisolvent. Afterward, the substrate was annealed at 100°C for 10 min. For solar cell devices, the doped spiro-OMeTAD solution was spin-coated at 4000 rpm for 30 s. At last, Au electrodes were thermally evaporated to define an active area of 0.25 cm² for measurements in the dark.

Device Characterization

Dark $I - V$ characteristics were recorded with a 10 mV step at different scan rates (from 1 V/s to 50 mV/s) using an Autolab potentiostat. The instrument was driven by the NOVA 2.1.5 software and 3 cycles were recorded from each scan rate starting in a forward direction from 0 V to 1.5 V, followed by a reverse direction from 1.5 V to -1.5 V, and finally recovered to 0 V. For light characterizations, experimental measurements were carried out using a Metrohm AutoLab optical bench with a blue LED (470 nm) as a light source. The distance between the sample and LED was adjusted to obtain 100 mW/cm² at a certain LED current and a complete light calibration was made using a Si photodiode. The LED was driven using an Autolab LED driver through the Autolab potentiostat. $I - V$ characteristics at different illumination intensities were measured from 10 to 100 mW/cm² using the same procedure followed for dark experiments. During light measurement, a mask was used to ensure a 0.1 cm² illumination area.

REFERENCES

- Almora, O., Aranda, C., Zarazua, I., Guerrero, A., and Garcia-Belmonte, G. (2016). Noncapacitive Hysteresis in Perovskite Solar Cells at Room Temperature. *ACS Energy Lett.* 1 (1), 209–215. doi:10.1021/acseenergylett.6b00116
- Alvarez, A. O., Arcas, R., Aranda, C. A., Bethencourt, L., Mas-Marzá, E., Saliba, M., et al. (2020). Negative Capacitance and Inverted Hysteresis: Matching Features in Perovskite Solar Cells. *J. Phys. Chem. Lett.* 11 (19), 8417–8423. doi:10.1021/acs.jpcclett.0c02331
- Aranda, C., Cristobal, C., Shoostari, L., Li, C., Huettner, S., and Guerrero, A. (2017). Formation Criteria of High Efficiency Perovskite Solar Cells under Ambient Conditions. *Sustain. Energy Fuels* 1, 540–547. doi:10.1039/c6se00077k
- Azpiroz, J. M., Mosconi, E., Bisquert, J., and De Angelis, F. (2015). Defect Migration in Methylammonium Lead Iodide and its Role in Perovskite Solar Cell Operation. *Energy Environ. Sci.* 8, 2118–2127. doi:10.1039/c5ee01265a
- Berruet, M., Pérez-Martínez, J. C., Romero, B., Gonzales, C., Al-Mayouf, A. M., Guerrero, A., et al. (2022). Physical Model for the Current-Voltage Hysteresis and Impedance of Halide Perovskite Memristors. *ACS Energy Lett.* 7, 1214–1222. doi:10.1021/acseenergylett.2c00121
- Bisquert, J., Cahen, D., Hodes, G., Rühle, S., and Zaban, A. (2004). Physical Mechanism Principles of Photovoltaic Conversion with Nanoparticulate, Mesoporous Dye-Sensitized Solar Cells. *J. Phys. Chem. B* 108, 8106–8118. doi:10.1021/jp0359283
- Bisquert, J., and Guerrero, A. (2022). Chemical Inductor. *J. Am. Chem. Soc.* 144, 5996–6009. doi:10.1021/jacs.2c00777
- Bisquert, J., and Guerrero, A. (2022). Dynamic Instability and Time Domain Response of a Model Halide Perovskite Memristor for Artificial Neurons. *J. Phys. Chem. Lett.* 13, 3789–3795. doi:10.1021/acs.jpcclett.2c00790

For IS measurements Autolab was configured to apply sinusoidal signals with a 10 mV amplitude from 1 MHz to 0.1 Hz under several illumination intensities and dc voltages, ranging from low to high illuminations and from 0 V to upper voltages. Chronoamperometry measurements during 20 s were carried out before and after IS.

DATA AVAILABILITY STATEMENT

The raw data supporting the conclusions of this article will be made available by the authors, without undue reservation.

AUTHOR CONTRIBUTIONS

LD, AR, RS, and AG made the measurements, AB and RJ were involved in conceptualization, BR, MK, AG, and JB planned the work, and AG and JB wrote the manuscript.

ACKNOWLEDGMENTS

The authors thank Generalitat Valenciana for the project PROMETEO/2020/028. A.B. acknowledges FPI studentship funding from Ministerio de Ciencia e Innovación of Spain (BES-2017-080351). R.A.J. acknowledges the support from the ETH Zurich Postdoctoral Fellowship scheme.

- Bisquert, J., Guerrero, A., and Gonzales, C. (2021). Theory of Hysteresis in Halide Perovskites by Integration of the Equivalent Circuit. *ACS Phys. Chem. Au* 1, 25–44. doi:10.1021/acspchemau.1c00009
- Bisquert, J. (2020). *The Physics of Solar Energy Conversion*. Boca Raton: CRC Press.
- Bou, A., and Bisquert, J. (2021). Impedance Spectroscopy Dynamics of Biological Neural Elements: From Memristors to Neurons and Synapses. *J. Phys. Chem. B* 125, 9934–9949. doi:10.1021/acs.jpcc.1c03905
- Bowring, A. R., Bertoluzzi, L., O'Regan, B. C., and McGehee, M. D. (2018). Reverse Bias Behavior of Halide Perovskite Solar Cells. *Adv. Energy Mat.* 8 (8), 1702365. doi:10.1002/aenm.201702365
- Caprioglio, P., Stolterfoht, M., Wolff, C. M., Unold, T., Rech, B., Albrecht, S., et al. (2019). On the Relation between the Open-Circuit Voltage and Quasi-Fermi Level Splitting in Efficient Perovskite Solar Cells. *Adv. Energy Mat.* 9 (33), 1901631. doi:10.1002/aenm.201901631
- Carrillo, J., Guerrero, A., Rahimnejad, S., Almora, O., Zarazua, I., Mas-Marza, E., et al. (2016). Ionic Reactivity at Contacts and Aging of Methylammonium Lead Triiodide Perovskite Solar Cells. *Adv. Energy Mat.* 6 (9), 1502246. doi:10.1002/aenm.201502246
- Christensen, D. V., Dittmann, R., Linares-Barranco, B., Sebastian, A., and Le Gallo, M. (2022). 2022 Roadmap on Neuromorphic Computing and Engineering. *Neuromorphic Comput. Eng.* 2, 022501. doi:10.1088/2634-4386/ac4a83
- Contreras, L., Idigoras, J., Todinova, A., Salado, M., Kazim, S., Ahmad, S., et al. (2016). Specific Cation Interactions as the Cause of Slow Dynamics and Hysteresis in Dye and Perovskite Solar Cells: A Small-Perturbation Study. *Phys. Chem. Chem. Phys.* 18 (45), 31033–31042. doi:10.1039/c6cp05851e
- Elbohy, H., El-Mahalawy, H., El-Ghamaz, N. A., and Zidan, H. (2019). Hysteresis Analysis in Dye-Sensitized Solar Cell Based on Different Metal Alkali Cations in the Electrolyte. *Electrochimica Acta* 319, 110–117. doi:10.1016/j.electacta.2019.06.160
- Emboras, A., Alabastri, A., Lehmann, P., Portner, K., Weilenmann, C., Ma, P., et al. (2020). Opto-Electronic Memristors: Prospects and Challenges in

- Neuromorphic Computing. *Appl. Phys. Lett.* 117 (23), 230502. doi:10.1063/5.0028539
- Fang, Y., Zhai, S., Chu, L., and Zhong, J. (2021). Advances in Halide Perovskite Memristor from Lead-Based to Lead-Free Materials. *ACS Appl. Mat. Interfaces* 13 (15), 17141–17157. doi:10.1021/acsami.1c03433
- Gogoi, H. J., Bajpai, K., Mallajosyula, A. T., and Solanki, A. (2021). Advances in Flexible Memristors with Hybrid Perovskites. *J. Phys. Chem. Lett.* 12 (36), 8798–8825. doi:10.1021/acs.jpcclett.1c02105
- Gong, J., Wei, H., Ni, Y., Zhang, S., Du, Y., and Xu, W. (2021). Methylammonium Halide-Doped Perovskite Artificial Synapse for Light-Assisted Environmental Perception and Learning. *Mater. Today Phys.* 21, 100540. doi:10.1016/j.mtphys.2021.100540
- Guerrero, A., Bisquert, J., and Garcia-Belmonte, G. (2021). Impedance Spectroscopy of Metal Halide Perovskite Solar Cells from the Perspective of Equivalent Circuits. *Chem. Rev.* 121, 14430–14484. doi:10.1021/acs.chemrev.1c00214
- Han, J. S., Le, Q. V., Choi, J., Kim, H., Kim, S. G., Hong, K., et al. (2019). Lead-Free All-Inorganic Cesium Tin Iodide Perovskite for Filamentary and Interface-Type Resistive Switching toward Environment-Friendly and Temperature-Tolerant Nonvolatile Memories. *ACS Appl. Mat. Interfaces* 11 (8), 8155–8163. doi:10.1021/acsami.8b15769
- John, R. A., Acharya, J., Zhu, C., Surendran, A., Bose, S. K., Chaturvedi, A., et al. (2020). Optogenetics Inspired Transition Metal Dichalcogenide Neuristors for In-Memory Deep Recurrent Neural Networks. *Nat. Commun.* 11 (1), 3211. doi:10.1038/s41467-020-16985-0
- John, R. A., Liu, F., Chien, N. A., Kulkarni, M. R., Zhu, C., Fu, Q., et al. (2018). Synergistic Gating of Electro-Iono-Photoactive 2D Chalcogenide Neuristors: Coexistence of Hebbian and Homeostatic Synaptic Metaplasticity. *Adv. Mat.* 30 (25), 1800220. doi:10.1002/adma.201800220
- John, R. A., Shah, N., Vishwanath, S. K., Ng, S. E., Febriansyah, B., Jagadeeswararao, M., et al. (2021). Halide Perovskite Memristors as Flexible and Reconfigurable Physical Unclonable Functions. *Nat. Commun.* 12 (1), 3681. doi:10.1038/s41467-021-24057-0
- John, R. A., Yantara, N., Ng, S. E., Patdillah, M. I. B., Kulkarni, M. R., Jamaludin, N. F., et al. (2021). Diffusive and Drift Halide Perovskite Memristive Barristors as Nociceptive and Synaptic Emulators for Neuromorphic Computing. *Adv. Mat.* 33 (15), 2007851. doi:10.1002/adma.202007851
- John, R. A., Yantara, N., Ng, Y. F., Narasimman, G., Mosconi, E., Meggiolaro, D., et al. (2018). Ionotronic Halide Perovskite Drift-Diffusive Synapses for Low-Power Neuromorphic Computation. *Adv. Mat.* 30 (51), 1805454. doi:10.1002/adma.201805454
- Juarez-Perez, E. J., Sanchez, R. S., Badia, L., Garcia-Belmonte, G., Kang, Y. S., Mora-Sero, I., et al. (2014). Photoinduced Giant Dielectric Constant in Lead Halide Perovskite Solar Cells. *J. Phys. Chem. Lett.* 5, 2390–2394. doi:10.1021/jz5011169
- Kang, K., Hu, W., and Tang, X. (2021). Halide Perovskites for Resistive Switching Memory. *J. Phys. Chem. Lett.* 12 (48), 11673–11682. doi:10.1021/acs.jpcclett.1c03408
- Kim, J. Y., Lee, J.-W., Jung, H. S., Shin, H., and Park, N.-G. (2020). High-Efficiency Perovskite Solar Cells. *Chem. Rev.* 120 (15), 7867–7918. doi:10.1021/acs.chemrev.0c00107
- Kim, M. S., Kim, M. S., Lee, G. J., Sunwoo, S.-H., Chang, S., Song, Y. M., et al. (2021). Bio-Inspired Artificial Vision and Neuromorphic Image Processing Devices. *Adv. Mater. Technol.* 7 (2), 2100144. doi:10.1002/admt.202100144
- Kwak, K. J., Lee, D. E., Kim, S. J., and Jang, H. W. (2021). Halide Perovskites for Memristive Data Storage and Artificial Synapses. *J. Phys. Chem. Lett.* 12 (37), 8999–9010. doi:10.1021/acs.jpcclett.1c02332
- Li, D., Wang, Y., Niu, T., Chao, L., and Chen, Y. (2022). Device Physics of a Metal Halide Perovskite Diode: Decoupling of the Bulk from the Interface. *J. Phys. Chem. C* 126 (15), 6892–6903. doi:10.1021/acs.jpcc.2c01568
- Lopez-Varo, P., Jiménez-Tejada, J. A., García-Rosell, M., Ravishankar, S., Garcia-Belmonte, G., Bisquert, J., et al. (2018). Device Physics of Hybrid Perovskite Solar Cells: Theory and Experiment. *Adv. Energy Mat.* 8, 1702772. doi:10.1002/aenm.201702772
- Ma, C., Chen, H., Yengel, E., Faber, H., Khan, J. I., Tang, M.-C., et al. (2021). Printed Memristor Utilizing a Hybrid Perovskite/Organic Heterojunction Channel. *ACS Appl. Mat. Interfaces* 13 (43), 51592–51601. doi:10.1021/acsami.1c08583
- Maier, P., Hartmann, F., Emmerling, M., Schneider, C., Kamp, M., Höfling, S., et al. (2016). Electro-Photo-Sensitive Memristor for Neuromorphic and Arithmetic Computing. *Phys. Rev. Appl.* 5 (5), 054011. doi:10.1103/physrevapplied.5.054011
- Mehonic, A., and Kenyon, A. J. (2016). Emulating the Electrical Activity of the Neuron Using a Silicon Oxide RRAM Cell. *Front. Neurosci.* 10, 57. doi:10.3389/fnins.2016.00057
- Li, D., Wang, Y., Niu, T., Chao, L., and Chen, Y. (2022). Device Physics of a Metal Halide Perovskite Diode: Decoupling of the Bulk From the Interface. *J. Phys. Chem.* 126, 6892–6903.
- Pershin, Y. V., and Di Ventra, M. (2011). Memory Effects in Complex Materials and Nanoscale Systems. *Adv. Phys.* 60 (2), 145–227. doi:10.1080/00018732.2010.544961
- Pockett, A., and Carnie, M. J. (2017). Ionic Influences on Recombination in Perovskite Solar Cells. *ACS Energy Lett.* 2 (7), 1683–1689. doi:10.1021/acscenergylett.7b00490
- Pospisil, J., Guerrero, A., Zmeskal, O., Weiter, M., Gallardo, J. J., Navas, J., et al. (2019). Reversible Formation of Gold Halides in Single-Crystal Hybrid-Perovskite/Au Interface upon Biasing and Effect on Electronic Carrier Injection. *Adv. Funct. Mat.* 29 (32), 1900881. doi:10.1002/adfm.201900881
- Rahimi Azghadi, M., Chen, Y.-C., Eshraghian, J. K., Chen, J., Lin, C.-Y., Amirsoleimani, A., et al. (2020). Complementary Metal-Oxide Semiconductor and Memristive Hardware for Neuromorphic Computing. *Adv. Intell. Syst.* 2 (5), 1900189. doi:10.1002/aisy.201900189
- Rong, Y., Hu, Y., Ravishankar, S., Liu, H., Hou, X., Sheng, Y., et al. (2017). Tunable Hysteresis Effect for Perovskite Solar Cells. *Energy Environ. Sci.* 10 (11), 2383–2391. doi:10.1039/c7ee02048a
- Senocrate, A., and Maier, J. (2019). Solid-State Ionics of Hybrid Halide Perovskites. *J. Am. Chem. Soc.* 141 (21), 8382–8396. doi:10.1021/jacs.8b13594
- Shastri, B. J., Tait, A. N., Ferreira de Lima, T., Pernice, W. H. P., Bhaskaran, H., Wright, C. D., et al. (2021). Photonics for Artificial Intelligence and Neuromorphic Computing. *Nat. Photonics* 15 (2), 102–114. doi:10.1038/s41566-020-00754-y
- Shen, H., Jacobs, D. A., Wu, Y., Duong, T., Peng, J., Wen, X., et al. (2017). Inverted Hysteresis in CH₃NH₃PbI₃ Solar Cells: Role of Stoichiometry and Band Alignment. *J. Phys. Chem. Lett.* 8 (12), 2672–2680. doi:10.1021/acs.jpcclett.7b00571
- Solanki, A., Guerrero, A., Zhang, Q., Bisquert, J., and Sum, T. C. (2020). Interfacial Mechanism for Efficient Resistive Switching in Ruddlesden-Popper Perovskites for Non-Volatile Memories. *J. Phys. Chem. Lett.* 11 (2), 463–470. doi:10.1021/acs.jpcclett.9b03181
- Stark, P., Horst, F., Dangel, R., Weiss, J., and Offrein, B. J. (2020). Opportunities for Integrated Photonic Neural Networks. *J. Nanophot.* 9 (13), 4221–4232. doi:10.1515/nanoph-2020-0297
- Tan, H., Liu, G., Yang, H., Yi, X., Pan, L., Shang, J., et al. (2017). Light-Gated Memristor with Integrated Logic and Memory Functions. *ACS Nano* 11 (11), 11298–11305. doi:10.1021/acsnano.7b05762
- Taukeer Khan, M., Khan, F., Al-Ahmed, A., Ahmad, S., and Al-Sulaiman, F. (2022). Evaluating the Capacitive Response in Metal Halide Perovskite Solar Cells. *Chem. Rec.*, e202100330. doi:10.1002/tcr.202100330
- Tress, W., Correa Baena, J. P., Saliba, M., Abate, A., and Graetzel, M. (2016). Inverted Current-Voltage Hysteresis in Mixed Perovskite Solar Cells: Polarization, Energy Barriers, and Defect Recombination. *Adv. Energy Mat.* 6 (19), 1600396. doi:10.1002/aenm.201600396
- Tress, W., Yavari, M., Domanski, K., Yadav, P., Niesen, B., Correa Baena, J. P., et al. (2018). Interpretation and Evolution of Open-Circuit Voltage, Recombination, Ideality Factor and Subgap Defect States during Reversible Light-Soaking and Irreversible Degradation of Perovskite Solar Cells. *Energy Environ. Sci.* 11 (1), 151–165. doi:10.1039/c7ee02415k
- Wetzelaer, G.-J. A. H., Scheepers, M., Sempere, A. M., Momblona, C., Ávila, J., and Bolink, H. J. (2015). Trap-Assisted Non-Radiative Recombination in Organic-Inorganic Perovskite Solar Cells. *Adv. Mat.* 27 (11), 1837–1841. doi:10.1002/adma.201405372
- Wu, F., Pathak, R., Chen, K., Wang, G., Bahrami, B., Zhang, W.-H., et al. (2018). Inverted Current-Voltage Hysteresis in Perovskite Solar Cells. *ACS Energy Lett.* 3 (10), 2457–2460. doi:10.1021/acscenergylett.8b01606
- Yang, G., Wang, C., Lei, H., Zheng, X., Qin, P., Xiong, L., et al. (2017). Interface Engineering in Planar Perovskite Solar Cells: Energy Level Alignment, Perovskite Morphology Control and High Performance Achievement. *J. Mat. Chem. A* 5 (4), 1658–1666. doi:10.1039/c6ta08783c
- Yang, J. J., Strukov, D. B., and Stewart, D. R. (2013). Memristive Devices for Computing. *Nat. Nanotech* 8 (1), 13–24. doi:10.1038/nnano.2012.240

Yang, X., Xiong, Z., Chen, Y., Ren, Y., Zhou, L., Li, H., et al. (2020). A Self-Powered Artificial Retina Perception System for Image Preprocessing Based on Photovoltaic Devices and Memristive Arrays. *Nano Energy* 78, 105246. doi:10.1016/j.nanoen.2020.105246

Zhang, T., Hu, C., and Yang, S. (2020). Ion Migration: A "Double-Edged Sword" for Halide-Perovskite-Based Electronic Devices. *Small Methods* 4 (5), 1900552. doi:10.1002/smt.201900552

Conflict of Interest: The authors declare that the research was conducted in the absence of any commercial or financial relationships that could be construed as a potential conflict of interest.

The handling editor MF declared a shared affiliation with the author(s) RE and MK at the time of review.

Publisher's Note: All claims expressed in this article are solely those of the authors and do not necessarily represent those of their affiliated organizations, or those of the publisher, the editors, and the reviewers. Any product that may be evaluated in this article, or claim that may be made by its manufacturer, is not guaranteed or endorsed by the publisher.

Copyright © 2022 Munoz-Diaz, Rosa, Bou, Sánchez, Romero, John, Kovalenko, Guerrero and Bisquert. This is an open-access article distributed under the terms of the Creative Commons Attribution License (CC BY). The use, distribution or reproduction in other forums is permitted, provided the original author(s) and the copyright owner(s) are credited and that the original publication in this journal is cited, in accordance with accepted academic practice. No use, distribution or reproduction is permitted which does not comply with these terms.